Monthly Notices of the ROYAL ASTRONOMICAL SOCIETY
MNRAS **501,** 4692–4702 (2021) doi:10.1093/mnras/staa2960

Analysis of wind-speed profiles and optical turbulence above Gaomeigu and the Tibetan Plateau using ERA5 data

Yajuan Han,[1,2,3] Qike Yang,[1,2,3] Nana Liu,[1,3,4] Kun Zhang,[1,3,4] Chun Qing,[1,3] Xuebin Li,[1,3] Xiaoqing Wu[1,3]★ and Tao Luo[1,3]★

[1]*Key Laboratory of Atmospheric Optics, Anhui Institute of Optics and Fine Mechanics, Chinese Academy of Sciences, Hefei, Anhui 230031, China*
[2]*Science Island Branch of Graduate School, University of Science and Technology of China, Hefei, Anhui 230026, China*
[3]*Advanced Laser Technology Laboratory of Anhui Province, Hefei 230037, China*
[4]*School of Environmental Science & Optoelectronic Technology, University of Science and Technology of China, Hefei, Anhui 230026, China*

Accepted 2020 September 16. Received 2020 September 16; in original form 2020 June 13

ABSTRACT

Appropriate knowledge of wind-speed distributions and optical turbulence at existing and potential astronomical observatories is crucial for siting ground-based telescopes and applying adaptive optics (AO) systems. In this paper, the wind-speed and optical-turbulence characteristics above Gaomeigu and the Tibetan Plateau are studied by employing the 20-yr (1999–2018) European Centre for Medium-Range Weather Forecasts' fifth set of reanalysis data (ERA5). First, the meteorological parameters derived from ERA5 data are evaluated with coinciding radiosonde measurements. Results show that the meteorological parameters of ERA5 data in the free atmosphere have quite good reliability, with bias and root mean square error basically lower than 1.2 K in temperature and basically smaller than 2 m s^{-1} for wind speed. Then, vertical distributions and seasonal behaviour of the wind speed at Gaomeigu and Lhasa station above the Tibetan Plateau are analysed. Thirdly, the Richardson number (R_i) in the free atmosphere is calculated to provides us with a map of relative probability of different periods and regions of optical turbulence being developed above the two sites. In general, the atmospheric stability of Gaomeigu is higher than that of Lhasa station. Particularly in June, for Gaomeigu, the atmospheric stability within 6–30 km a.s.l. is basically superior or equal to the stable condition found at two mid-latitude sites: Oukaimeden and La Palma. Moreover, Lhasa station has a relative higher stability during June–September than other months. Furthermore, we provide the (C_n^2) profiles using ERA5 data at Gaomeigu and Lhasa. The results indicate that the choice of an appropriate outer-scale model is crucial for revealing local turbulence characteristics.

Key words: turbulence – atmospheric effects – methods: data analysis – site testing.

1 INTRODUCTION

Optical turbulence, characterized by the refractive index structure parameter (C_n^2) (Tatarskii 1961), affects the propagation of laser beams and observation by ground-based telescopes (Fried 1966; Hutt 1999). In terms of optical astronomy, atmospheric turbulence severely limits the angular resolution of optical telescopes and causes motion and blurring of the stellar image (Roddier 1981; Vernin 1986).

As a fundamental factor to trigger optical turbulence, wind speed plays a crucial role in optical astronomy. Wind speed is closely related to the strength of optical turbulence: the stronger the intensity of the wind-speed gradient, the larger the probability that turbulence will be triggered. In addition, if the wind speed is stronger, the velocity of the atmospheric turbulence layer passing through the telescope pupil will be higher. Therefore, adaptive optics (AO) systems must work at higher frequencies to correct the turbulent disturbances above the wavefront. Moreover, a high wind speed near the ground will cause vibrations in telescope structures. Wind speed at the 200 hPa pressure level (hereafter V_{200}) is considered a parameter in evaluating the features of astronomical sites (Sarazin & Tokovinin 2002; García-Lorenzo et al. 2005, 2009). This is supported by the similar seasonal variation between V_{200} and seeing at Mauna Kea and La Silla (Vernin 1986). However, later, it was proved that only using V_{200} to characterize a site was insufficient, and researchers proposed that vertical profiles of wind speed were fundamental and necessary in astronomical site evaluation and astronomical applications (García-Lorenzo et al. 2009; Hagelin, Masciadri & Lascaux 2010; Masciadri et al. 2010; Bolbasova et al. 2019). In terms of its importance, some astronomical sites have investigated the vertical distribution of wind speed to evaluate site characteristics (Masciadri & Garfias 2001; García-Lorenzo et al. 2005; Avila et al. 2006; Egner, Masciadri & McKenna 2007; Hagelin et al. 2010; Hach et al. 2012). Therefore, appropriate knowledge of wind-speed vertical distributions is essential to provide help in site evaluation and selection of ground-based telescopes, further to support the application of AO facilities and to arrange the scheduling of scientific programmes.

There are several techniques to detect vertical profiles of wind speed, such as balloon-borne radiosonde, generalized SCIDAR (scintillation detection and ranging; GS) and single-star SCIDAR. Meteorological balloons equipped with GPS and microthermometers can directly detect wind-speed profiles with high vertical resolution (typically a few metres) during each flight (Azouit & Vernin 2005), and they have been widely used in different field campaigns

★ E-mail: xqwu@aiofm.ac.cn (XW); luotao@aiofm.ac.cn (TL)

(Abahamid et al. 2004; Wu et al. 2014; Cai et al. 2018; Han et al. 2020). Moreover, GS, on the basis of the remote optical sensing principle, can reconstruct vertical profiles of wind speed at each turbulent layer (Vernin & Azouit 1983; Avila, Vernin & Sánchez 2001). In recent years, some observations have been carried out at different sites employing GS (Avila et al. 2006; Egner et al. 2007; Masciadri et al. 2010). Subsequently, based on a similar principle, single-star SCIDAR has been used to deduce the wind-speed profile by analysing the scintillation of a single star (Caccia, Azouit & Vernin 1987; Habib, Vernin & Benkhaldoun 2005).

However, these techniques are expensive and require professional technology in their usage. Moreover, it is difficult to carry out long-term *in situ* measurements due to tremendous expenses and existing observation difficulties, especially for locations at high altitudes. Alternatively, with the auspices of the Copernicus Climate Change Service (C3S), the fifth European Centre for Medium-Range Weather Forecasts Reanalysis (ERA5) produced by the European Centre for Medium-Range Weather Forecasts (ECMWF), with high spatial and temporal resolution, is a simple way to provide the site characteristics using long temporal atmospheric parameters, such as wind speed and absolute temperature.

In recent years, the Tibetan Plateau has attracted extensive interest from astronomers for ground-based optical telescope observations due to its high elevation and unique weather regimes (Huang 1996; Zhang et al. 2010; Liu et al. 2012; Stone 2012; Yao et al. 2012, 2015; Ye et al. 2016; Kuo 2017; Qian et al. 2018). Gaomeigu, the site of a 2.4-m telescope, which is the largest general-use optical telescope in China, is located at 26.70°N, 100.03°E, at an altitude of approximately 3200 m above sea level (a.s.l.) in Lijiang, Yunnan province, China. As there are few astronomical observatories around the world near the same longitute, Gaomeigu is playing an increasingly important role in international astronomical observations. So far, a series of scientific achievements have been made using the Lijiang 2.4-m telescope (Venemans 2015; Wu et al. 2015; Wang et al. 2019). However, up to now, there has been no systematic and complete research into the vertical distribution of wind speed above the Tibetan Plateau and Gaomeigu. For the Tibetan Plateau in particular, the adverse weather and harsh enviromental factors cause a scarcity of *in situ* observations in this region. Knowledge of this distribution will help us to identify the regional characteristics of wind speed at different pressure levels and to master the local atmospheric conditions. Moreover, we can obtain preliminary turbulence information from atmospheric parameters, especially the wind speed. Therefore, in this study, we present a first attempt to assess the site features above Gaomeigu and the Tibetan Plateau over a 20-yr time-scale using vertical distributions of wind speed retrieved from ERA5 data.

Furthermore, comparing the Richardson number (R_i) over different locations helps us to provide a relative evaluation of which location is more or less likely to produce optical turbulence (Geissler & Masciadri 2006; Hagelin et al. 2008). Using $1/R_i$ as a qualitative relative indicator to rank locations according to their likelihood of producing optical turbulence is presented in Geissler & Masciadri (2006); it was then substantiated by Hagelin et al. (2008) when comparing Mt Graham and Dome C. Subsequently, it was applied to different comparisons, such as on the Antarctic Plateau – the South Pole, Dome C, and Dome A (Hagelin et al. 2008) – and at two mid-latitude sites, Oukaimeden and La Palma (Hach et al. 2012).

We propose three scientific goals in our study as follows:

First, we evaluate the reliability of the ERA5 data and provide an overall statistical analysis by comparing the vertical profiles of atmospheric parameters (absolute temperature and wind speed) retrieved from the ERA5 archives with the coinciding radiosonde observations.

Secondly, we present the first complete seasonal investigation of the vertical wind-speed distribution at Gaomeigu and Lhasa station above the Tibetan Plateau in each individual month of the year for the period of 1999–2018 using ERA5 data. The seasonal behaviour of wind speed is also investigated. In addition, we provide a statistical analysis of monthly average wind speed at the 200 hPa pressure level.

Finally, we conduct a comparision of stable and unstable conditions of the free atmosphere and discuss the possibility of atmospheric turbulence being triggered using the Richardson number (R_i) maps for the two sites, Gaomeigu and Lhasa station. We intend to evaluate the atmospheric characteristics of the two sites. In addition, we display the profiles of optical-turbulence strength determined from the ERA5 system.

2 DATA

2.1 ERA5 data

ERA5 is ECMWF's latest set of global reanalysis data, which replaces the ERA-Interim product and will be publicly available with data from 1950 onwards once completed (Hersbach et al. 2020). Based on the 4D-Var data assimilation method, ERA5 uses Cycle 41r2 of the Integrated Forecasting System (IFS). It presents global data with flexible options of regions for a long time period, which is the assimilation of different types of observations. These data contain a variety of atmospheric quantities, such as absolute temperature, relative humidity, and horizontal components of wind speed (u and v). Beyond ERA5, several global atmospheric reanalyses have been produced by different groups; the most recent being the MERRA-2 (Modern-Era Retrospective analysis for Research and Applications, version 2) reanalysis (Gelaro et al. 2017) produced by the NASA GMAO (National Centers for Atmospheric Research Global Modeling and Assimilation Office), JRA-55 (Japanese 55-yr) reanalysis (Kobayashi et al. 2015) from the JMA (Japan Meteolorogical Agency), and CFSv2 (Climate Forecast Systeam Reanalysis, version 2) from NCEP (National Centers for Environmental Prediction) (Saha et al. 2014). Compared with these global reanalysis products, higher temporal and spatial resolution is the major strength of ERA5 (Hersbach et al. 2020). A horizontal resolution of 31 km, 137 vertical pressure levels from the surface to 0.01 hPa, and hourly output capture more details of atmospheric parameters than previous lower-resolution global reanalyses. Moreover, the large number of assimilated data sets is also a crucial improvement over other reanalyses.

2.2 Radiosonde data

The Integrated Global Radiosonde Archive version 2 (IGRAv2) (Durre et al. 2016) is a comprehensive and free-access radiosonde data set produced by the National Climatic Data Center (NCDC). It contains quality-assured observations at stations across all continents during different periods, some of which cover the period from the 1960s to the present. Observations include geopotential height, atmospheric temperature, and horizontal wind speed (u and v) at different mandatory pressure levels. Radiosondes generally are released twice daily at 00:00 and 12:00 UTC, respectively.

The preliminary surveys of Gaomeigu as a promising site for observational astronomy were provided by Ma et al. (1996), Zhang, Yu & Tan (1996), and Qian et al. (1996). Subsequently, numerous researchers conducted a set of investigations concerning site evaluation at Gaomeigu, such as seeing, astro-climatic conditions,

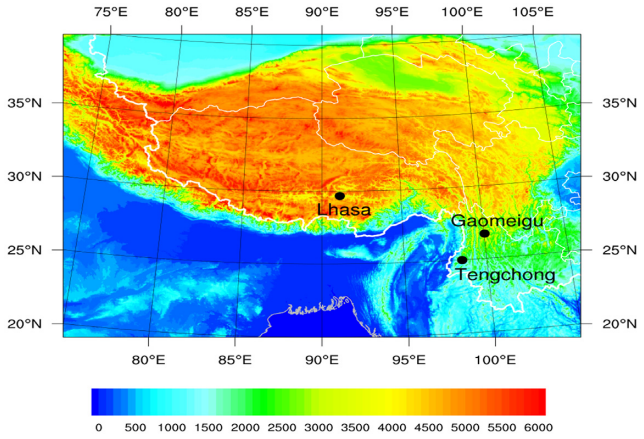

Figure 1. Topographic map (altitude in metres) of Lhasa, Gaomeigu, and Tengchong stations; black dots denote the Lhasa, Gaomeigu, and Tengchong stations, respectively.

and photometric qualifications (Yu et al. 1996; Liu et al. 1999; Yunnan Observatory Site Survey Group 1999a, 1999b; Cen et al. 2002; Qian et al. 2002). These results demonstrated that Gaomeigu was worth choosing as a good observing site. Therefore, the first optical telescope, the 2.4-m telescope, was installed at Gaomeigu (Li & Qian 2005). Due to the lack of large independent observations at Gaomeigu, Tengchong station, which is the closest radiosonde station in IGRAv2 to Gaomeigu, is used to verify the validity of the ERA5 data in this region.

The Tibetan Plateau (called 'the roof of the world') over Asia is the highest and largest plateau in the world, with an average altitude of more than 4500 m and an area coverage of 2.5 million km^2. It influences the weather and climate over East Asia through atmospheric circulation because of the dynamic and thermal effects triggered by high and complex terrains (Ding & Chan 2005; Bao, Zhang & Sun 2011). Lhasa Meteorological Station (91.13°E, 29.67°N) is located in the Tibetan Plateau, with an altitude about 3650 m a.s.l. In this study, we use the radiosonde data of Lhasa station in IGRAv2 to evaluate the ERA5 data. The locations and topographic distribution of Lhasa, Gaomeigu, and Tengchong stations are shown in Fig. 1.

3 EVALUATION OF ERA5 DATA

The evaluation of ERA5 data at Tengchong and Lhasa stations is investigated, by making a comparison using the monthly mean data during 2016–2018 between the observations obtained from IGRAv2 and the simulations extracted from ERA5 data closest to Tengchong and Lhasa stations, respectively. We have eliminated the profiles of IGRAv2 that do not exceed 20 km a.s.l. The corresponding geographic coordinates are given in Table 1.

In order to quantify the statistical reliability of ERA5 data in reconstructing the profiles of classical atmospheric parameters (absolute temperature and wind speed), two statistical operators (Masciadri, Lascaux & Fini 2013) including the bias and the root mean square error (RMSE) are used.

3.1 Evaluation of ERA5 data at Tengchong station

The bias, the RMSE, and the average vertical profiles of absolute temperature and wind speed at Tengchong in the 3.1–26.3 km a.s.l. range are depicted in Fig. 2. In detail, the vertical profiles of different meteorological parameters of observations and simulations were interpolated to 100 m, then the bias, RMSE, and average were calculated at each interpolated height; finally a moving average with 1 km was used in the resulting profiles of bias and RMSE.

For the absolute temperature, the absolute value of bias is not greater than 0.6 K, with an RMSE that is not more than 0.8 K. For the wind speed, we note that the absolute value of bias never exceeds 1.5 m s^{-1}, and the RMSE is lower than 2 m s^{-1}.

3.2 Evaluation of ERA5 data at Lhasa station above the Tibetan Plateau

Meanwhile, in the same way, the overall statistics of ERA5 data at Lhasa station above the Tibetan Plateau between 5.8 and 25.9 km a.s.l. is also performed, as displayed in Fig. 3.

In the absolute temperature, the absolute value of bias and the RMSE rarely exceed 1.2 K. For the wind speed, the absolute value of bias and the RMSE are basically never greater than 1.5 m s^{-1} and 2 m s^{-1}, respectively.

In conclusion, the overall statistical results reveal that the absolute temperature and wind speed in the free atmosphere retrieved from ERA5 data are reliable and satisfactory and may suffice to evaluate the site characterization in terms of optical-turbulence parameters.

4 WIND-SPEED DISTRIBUTION AND SEASONAL BEHAVIOUR

In this section, we use the ERA5 data to investigate the characteristics of wind speed concerning monthly distribution and seasonal fluctuations at Gaomeigu and Lhasa station above the Tibetan Plateau on a 20-yr time-scale, from 1999 to 2018. Allowing for the difference in altitude between the ERA5 grid point (∼3.1 km for Gaomeigu, ∼3.7 km for Lhasa station) and the summit of Gaomeigu (3200 m) as well as Lhasa station (3650 m), we study the results between 650 hPa (∼3.7 km a.s.l.) and 30 km a.s.l. (∼10 hPa) at Gaomeigu, and between 600 hPa (∼4.3 km a.s.l.) and 30 km a.s.l. (∼10 hPa) at Lhasa station.

Fig. 4 displays the monthly median vertical distributions of wind speed at Gaomeigu and Lhasa station during the period 1999–2018. The first and third quartiles are marked with dotted lines.

For Gaomeigu and Lhasa station, during autumn to spring but excluding September (the beginning of autumn), the vertical profiles of wind speed at around 12 km a.s.l. show typical characteristics of a mid-latitude site, i.e. the maximum wind speed appears at jet-stream level (200 hPa). During the same period, the maximum median wind speed at jet-stream level is about 52.92 m s^{-1} in January for Gaomeigu and roughly 53.60 m s^{-1} in December for Lhasa station, while the minimum is 22.57 m s^{-1} in October for Gaomeigu and 28.56 m s^{-1} in May for Lhasa station. In May and October, the wind-speed profiles show the same trend, with the first peak at jet-stream height larger than the second peak at about 25 km a.s.l.; and the wind-speed value at the second peak is not greater than 10 m s^{-1} for the two sites.

Compared with other months, wind speeds are weaker and show different trends in summer and September for the two sites. In July and August, the wind speed increases with altitude well into the stratosphere, and reaches about 25 m s^{-1} at 30 km a.s.l. For Gaomeigu, in June and September, below 12 km a.s.l., we observe that the wind speed remains quite weak and rises more slowly than that in any other month; in September in particular the maximum median wind speed is not greater than 5 m s^{-1}. In the 15–30 km a.s.l. range, the median wind speed increases with altitude and never exceeds 17 m s^{-1} at Gaomeigu. For Lhasa station, in June and

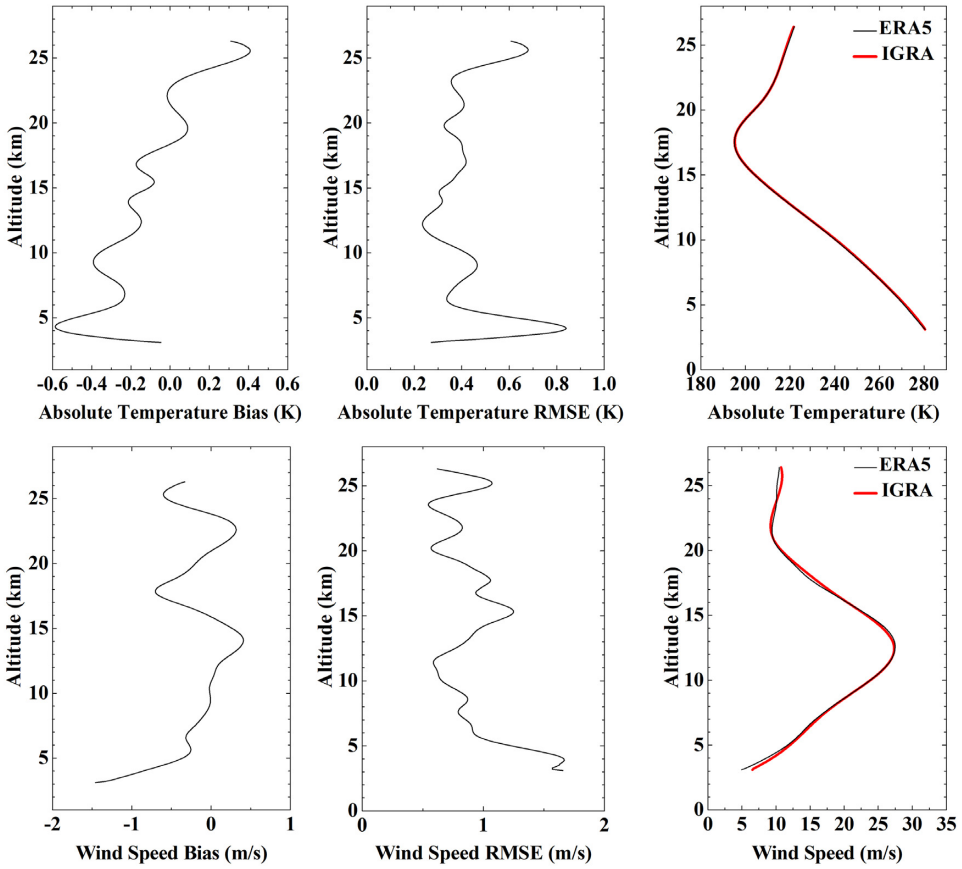

Figure 2. First, second, and third columns: bias and RMSE (ERA5 data minus observations) and average profiles of absolute temperature and wind speed for Tengchong. In the third column, the thick lines represent observations acquired from IGRAv2 and the thin lines represent estimations retrieved from ERA5 data. On the *y*-axis, *h* between 3.1 and 26.3 km a.s.l. is reported.

September, above a height of 20 km a.s.l., the median wind speed increases with altitude and reaches a value comparable to V_{200} but its intensity is basically lower than 15 m s^{-1}.

The interquartile range indicates the year-to-year variability of profiles of wind speed (Bolbasova et al. 2019). Two large dispersions of the interquartile range can be observed at the two sites; that is, the differences between the values of the first and third quartiles are over 5 m s^{-1}. One is situated at the jet-stream level during winter, spring, and October and the other is centred around 25 km a.s.l. during December and January. In general, the wind speeds over Gaomeigu and Lhasa station have not changed much in the past 20 years.

In conclusion, for the two sites, we can see significant seasonal behaviour of wind-speed intensity, with stronger wind speeds in winter and weaker ones in summer and September. Moreover, for the two sites, the wind-speed characteristics during winter, spring, October, and November show a similar trend, while the wind-speed characteristics in July and August show another trend. During January to April and July and August, the intensity of wind speed at Lhasa station is basically lower than or equal to that of Gaomeigu, but in May, June, and September to December, there are complex relationships between the wind-speed intensity above the two sites.

To further demonstrate the seasonal behaviour of wind speed at jet-stream level, we present the monthly averages of V_{200} at Gaomeigu and Lhasa station during 1999–2018, as shown in Fig. 5. For the two sites, the variations of V_{200} indicate clear seasonal behaviour at this specific height (about 12 km a.s.l.). The specific wind-speed values are shown in Tables A1 and A2 in the Appendix A (which is available as supplementary material), including heights and average values. The highest and lowest average V_{200} are observed in January (53.02 m s^{-1}) and September (4.83 m s^{-1}) for Gaomeigu, and in January (53.57 m s^{-1}) and July (4.74 m s^{-1}) for Lhasa station.

5 ESTIMATION OF OPTICAL TURBULENCE IN THE FREE ATMOSPHERE

5.1 Richardson number R_i

The strength of optical turbulence is a fundamental parameter in astronomical site evaluation. The instability of atmosphere is closely related to the generation of optical turbulence. The Richardson number R_i represents the stability or instability features of the atmosphere.

$$R_i = \frac{g}{\theta}\frac{\partial\theta/\partial h}{(\partial V/\partial h)^2}, \tag{1}$$

where g is 9.8 m s^{-2}, θ is the potential temperature, and V is the horizontal wind speed. The gradient of the horizontal wind speed is defined as:

$$\frac{\partial V}{\partial h} = \sqrt{\left(\frac{\partial u}{\partial h}\right)^2 + \left(\frac{\partial v}{\partial h}\right)^2}, \tag{2}$$

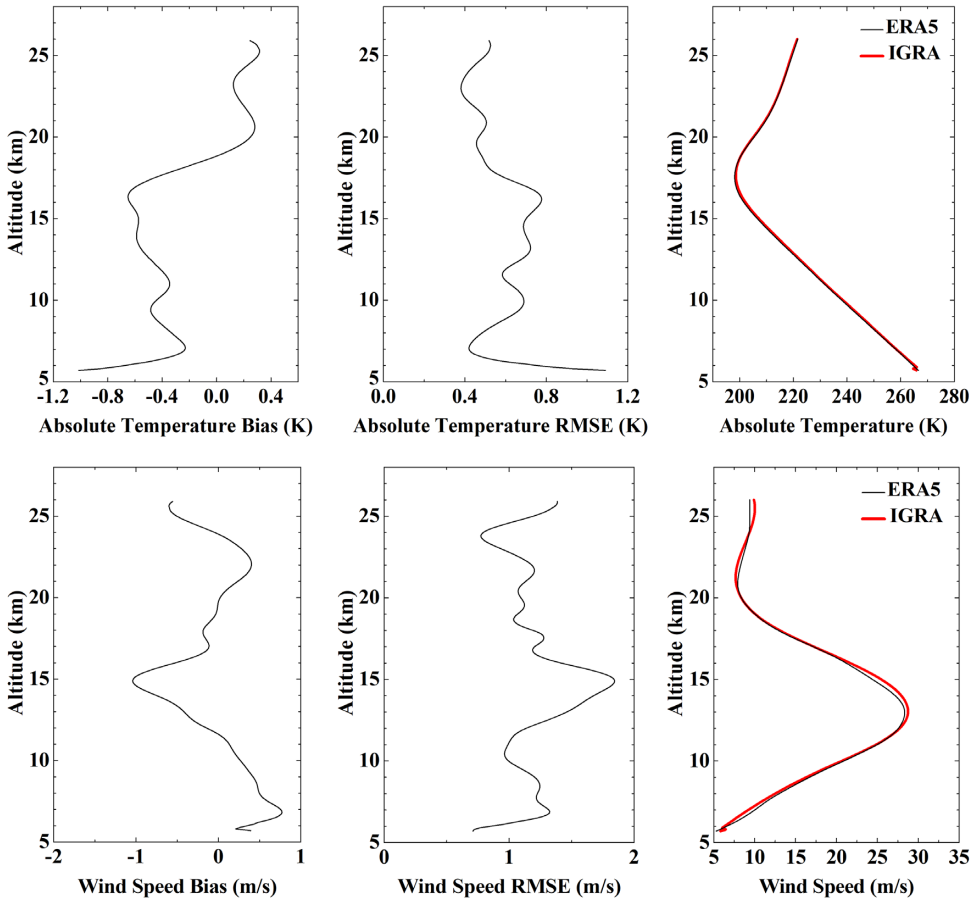

Figure 3. First, second, and third columns: bias and RMSE (ERA5 data minus observations) and average profiles of absolute temperature and wind speed at Lhasa station above the Tibetan Plateau. In the third column, the thick lines represent observations acquired from IGRAv2 and the thin lines represent estimations extracted from ERA5 data. On the *y*-axis, *h* between 5.8 and 25.9 km a.s.l. is reported.

where u and v are two components of horizontal wind speed. In this section, we evaluate the possibility of where and when the optical turbulence occurs and compare the level of relative stability or instability of the free atmosphere using $1/R_i$ profiles for each month during 1999–2018 above the two sites, Gaomeigu and Lhasa station. Results are calculated based on temperature and wind speed extracted from ERA5 archives, in the 650 hPa (about 3.7 km) − 30 km range above Gaomeigu and in the 600 hPa (about 4.3 km) − 30 km range above Lhasa station, respectively.

The occurrence of atmospheric turbulence requires certain dynamic and thermal instabilities. The thermal instability can be estimated by the gradient of potential temperature (when $\partial\theta/\partial h > 0$) and the dynamic instability can be identified by R_i. The atmosphere is classified as stable when R_i is larger than 1/4, and as unstable when R_i is smaller than 1/4; that is, atmospheric turbulence is more easily triggered when R_i is small. However, the atmosphere is dominated by stable conditions at night and it is hard to detect dynamic instabilities induced by strong wind-speed shear. Masciadri & Garfias (2001) follow a statistical method (VanZandt et al. 1978; VanZandt, Gage & Warnock 1981) to figure out a more reasonable criterion to displace R_i, using the probability density function obtained from atmospheric parameters with a low spatial resolution to characterize the instability and stability conditions of the atmosphere. In addition, the probability density function for describing the dynamical instability in the atmosphere is based on the vertical gradient of potential temperature ($\partial\theta/\partial h$) and wind speed ($\partial V/\partial h$) over large spatial scales (a few kilometres) (VanZandt et al. 1978). Conventional instability conditions are employed, which can be triggered when $\partial V/\partial h \geq 1$ and $\partial\theta/\partial h < 1$, or $\partial\theta/\partial h \sim 0$.

Figs 6 and 7 display the monthly median gradient of the potential temperature ($\partial\theta/\partial h$) and square of the gradient of the wind speed ($(\partial V/\partial h)^2$), respectively. Furthermore, for each single month the median inverses of the Richardson numbers ($1/R_i$) of Gaomeigu and Lhasa station are shown in Fig. 8. Gaomeigu is marked with a dark line and Lhasa station with a red line. We replace R_i with $1/R_i$ because $1/R_i$ can represent the possible regions of optical-turbulence production over a better dynamic range.

From Fig. 6, the value of $\partial\theta/\partial h$ is basically lower than 0.01 K m^{-1} below 12 km a.s.l. at the two sites, Gaomeigu and Lhasa station. In summer and September, the profiles of $\partial\theta/\partial h$ are identical above 7 km a.s.l. and show almost the same smallest value around 12 km a.s.l. for the two sites. During autumn to spring, except in September, the vertical profiles of $\partial\theta/\partial h$ show a different trend at the two sites, especially below 15 km a.s.l.

In Fig. 7, during autumn to spring, except in September, the vertical profiles of $(\partial V/\partial h)^2$ at the two sites present a similar trend, that is, with two distinct peaks. The position of the first peak at the two sites is closer, approximately located at 15–17 km a.s.l., while the position of the second peak is a little far away. The first peak corresponds to the decrease in wind speed above the jet-stream level, and the second peak corresponds to the increase in wind speed below the jet-stream level. The value of $(\partial V/\partial h)^2$ at the dividing point of the two peaks is

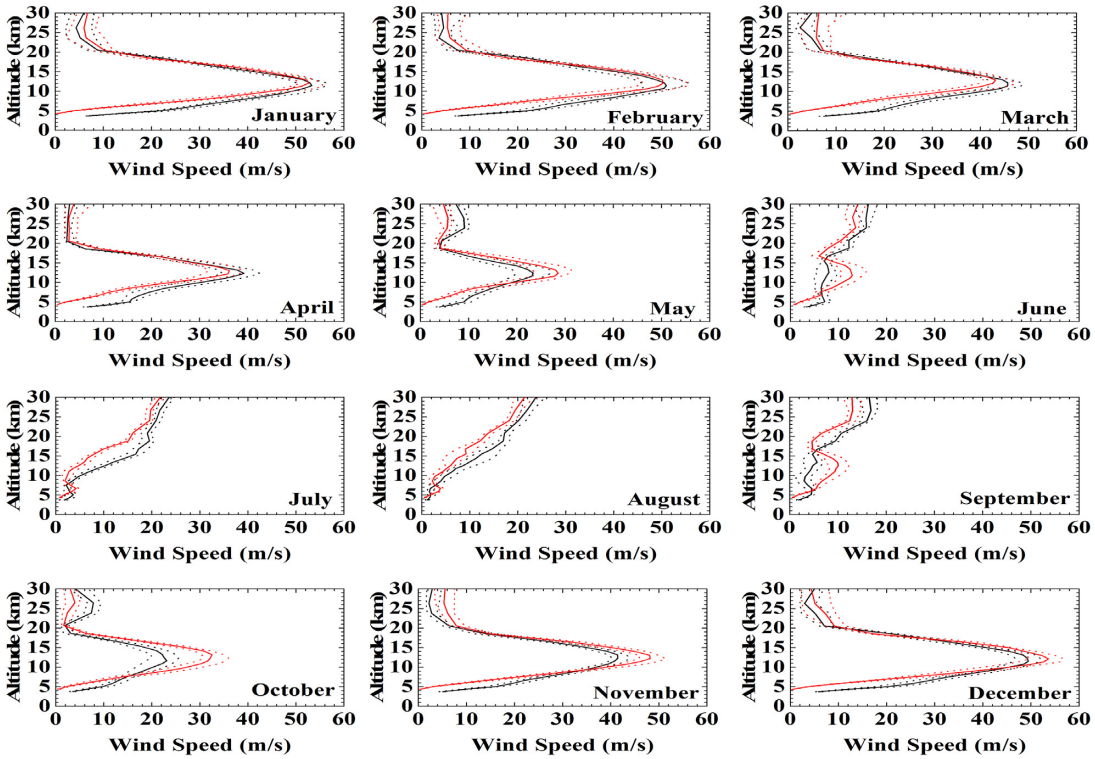

Figure 4. The monthly median vertical profiles of wind speed during 1999–2018 at Gaomeigu (dark lines) and Lhasa station (red lines). The dashed lines represent the first and third quartiles.

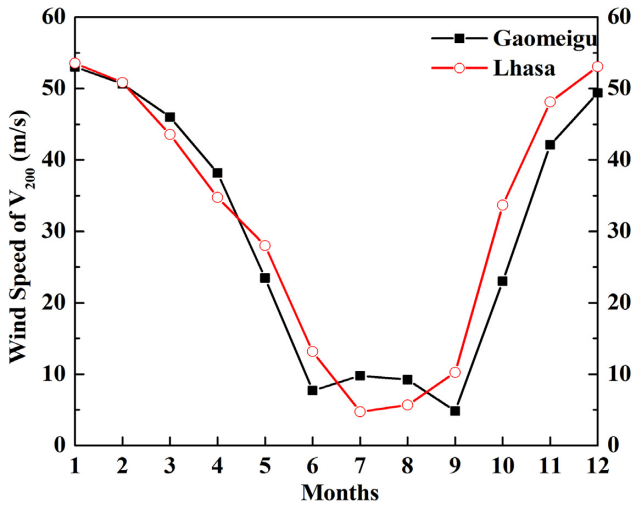

Figure 5. Monthly average of wind speed at 200 hPa from ERA5 data during 1999–2018 at Gaomeigu and Lhasa station.

the minimum, corresponding to the position of the jet stream, where the median wind speed is the largest. In particular, the positions of the two peaks in April and May are almost at the same height at the two sites, respectively. During the same period, the profile intensities of $(\partial V/\partial h)^2$ over Gaomeigu are basically inferior to or equal to those observed over Lhasa station above 6 km a.s.l.

During summer and September, the profile intensity of $(\partial V/\partial h)^2$ above the two sites is obviously smaller than those in other months, which is caused by the weaker monthly median wind speed. In addition, the profiles of $(\partial V/\partial h)^2$ above Gaomeigu and Lhasa show complex features.

In Fig. 8, according to the $1/R_i$ value in different months, the $1/R_i$ profiles can be divided into two periods, where R_i shows similar features.

During autumn to spring, except in September, there are two regions with particularly large $1/R_i$ for the two sites. The instability, i.e. large $1/R_i$, is closely associated with the existing conditions of $\partial\theta/\partial h$ and $(\partial V/\partial h)^2$ mentioned above. The first large value of $1/R_i$ is observed at around 15–17 km a.s.l. One can note that the strong intensity of $1/R_i$ is caused by the large intensity of $(\partial V/\partial h)^2$ and low intensity of $\partial\theta/\partial h$. Below 10 km, $1/R_i$ presents a second large intensity, which is equal or superior to the observed first one, corresponding to the height where $\partial\theta/\partial h \sim 0$. Therefore, with the instability conditions of the two regions, the possibility that optical turbulence is produced may be larger.

During summer and September, the stability (low $1/R_i$) of the two sites is significantly larger than that of other months. It is worth noting that the extremely low intensity of $1/R_i$ in June and September at Gaomeigu indicates the most stable condition in all months. Particularly in June, the stability of the atmosphere at Gaomeigu within 6–30 km a.s.l. is basically superior or equal to the most stable condition of the atmosphere found at two mid-latitude sites, Oukaimeden in July and October and La Palma in August and October during the same period (see Fig. B1 in Appendix B, which is available as supplementary material).

Above 20 km a.s.l., the intensity of $1/R_i$ remains very low for the two sites, indicating stable conditions in the atmosphere. In general, except for July and August, the level of stability of the atmosphere at Gaomeigu is basically higher than that of Lhasa station above 6 km a.s.l.

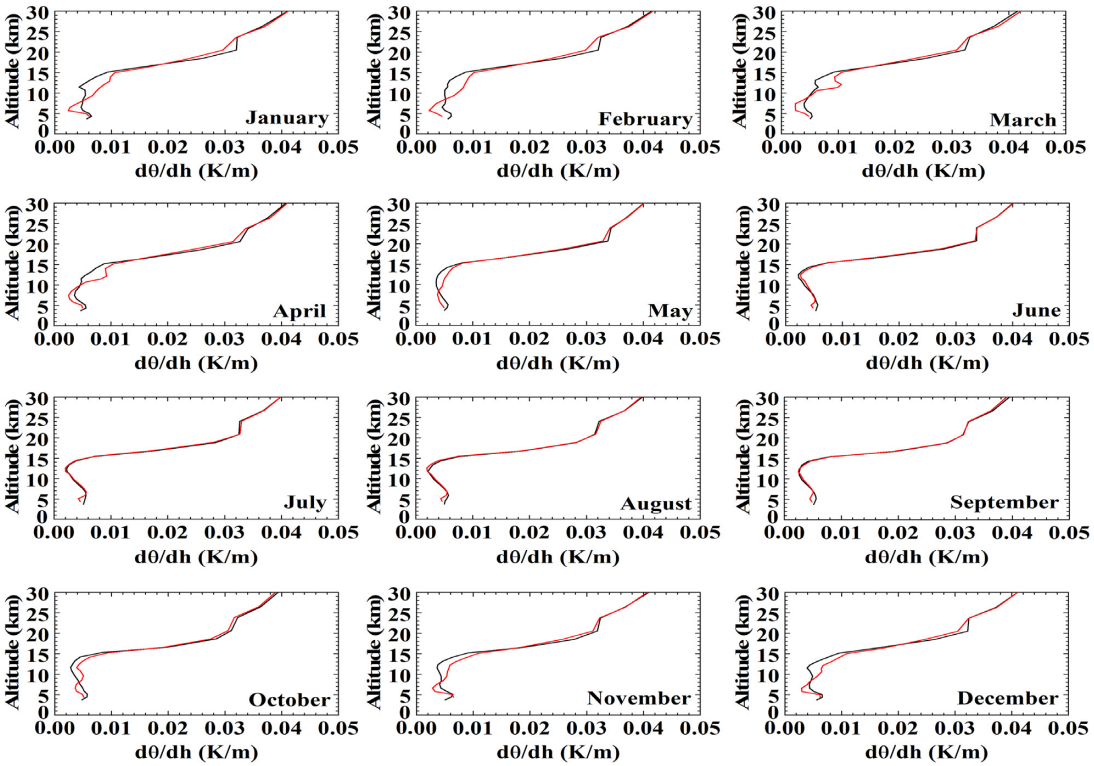

Figure 6. The monthly median vertical profiles of $\partial\theta/\partial h$ obtained from ERA5 data during 1999–2018 for Gaomeigu (dark lines) and Lhasa station (red lines).

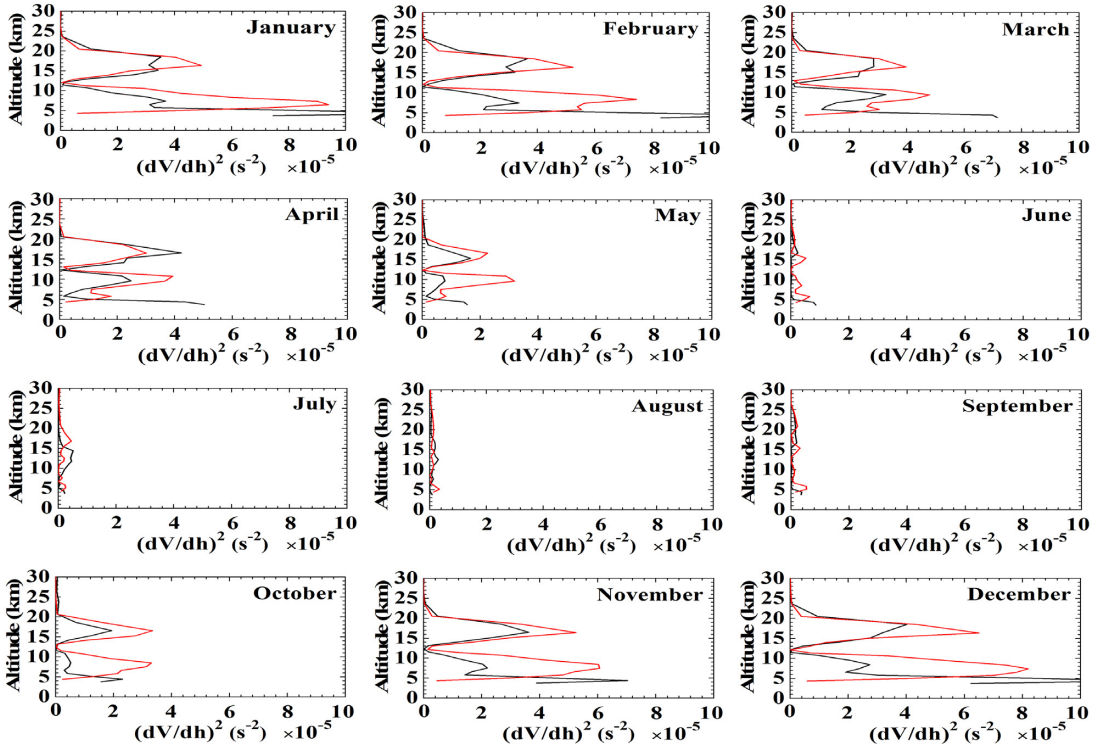

Figure 7. The monthly median vertical profiles of $(\partial V/\partial h)^2$obtained from ERA5 during 1999–2018 for Gaomeigu (dark lines) and Lhasa station (red lines).

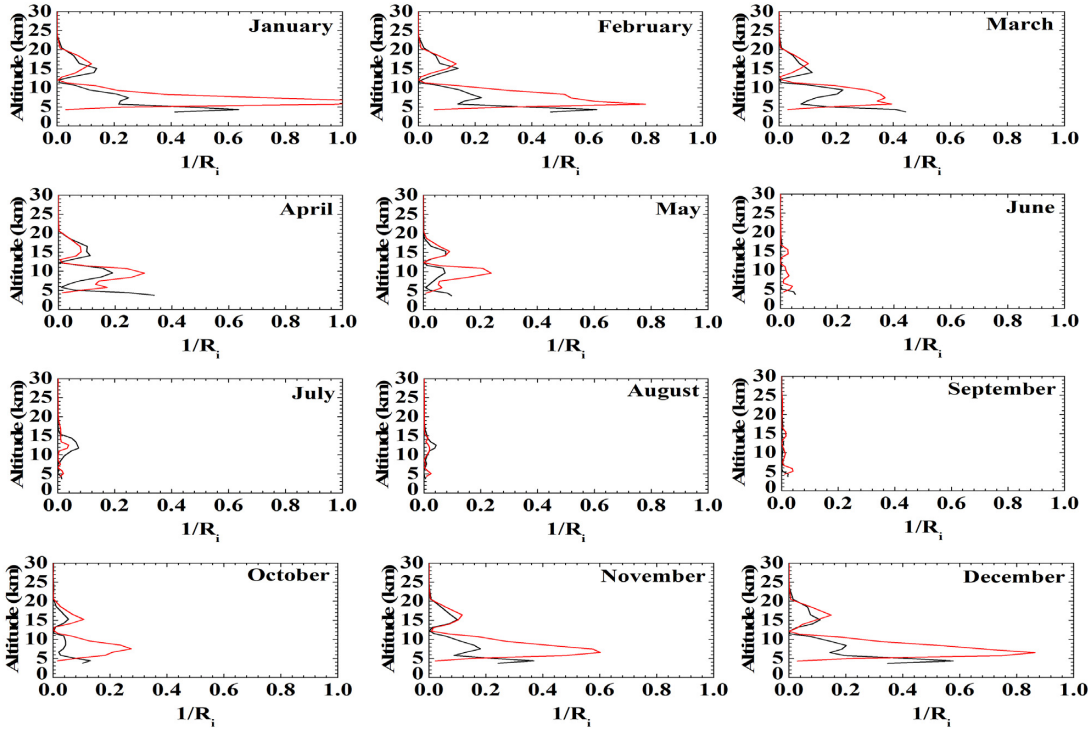

Figure 8. The monthly median vertical profiles of $1/R_i$ obtained from ERA5 during 1999–2018 for Gaomeigu (dark lines) and Lhasa station (red lines).

Table 1. The geographic coordinates of Tengchong and Lhasa stations and the corresponding nearest grid points extracted from ERA5 data.

Site	Elevation (m)	Latitude (°)	Longitude (°)
Tengchong	1697	24.98°N	98.51°E
		25.00°N	98.50°E
Lhasa station	3650	29.67°N	91.13°E
		29.55°N	91.05°E

The map of $1/R_i$ cannot provide us with the specific turbulence strength at a certain height, but it can help us to compare the relative conditions of atmospheric stability between different sites. For Gaomeigu and Lhasa station, we can identify the likely periods and regions that show instability over two ranges in the free atmosphere. General stability exists at the two sites above 20 km a.s.l. For the two sites, a higher stability during summer and September is found than in other months. During autumn to spring, except for September, all the months have similar atmospheric stability characteristics. One can see that the relative comparison between the two sites in terms of optical turbulence indicates that Gaomeigu is accompanied by more stable conditions than Lhasa station. In addition, the atmospheric stability of Gaomeigu in June and September is favourable for astronomical applications.

We find that Qian et al. (2002) and Cen et al. (2002) have investigated the seeing or Fried parameter at Gaomeigu. Thus, we show their results in Tables 2 and 3, respectively. Despite the lack of seeing in the free atmosphere at Gaomeigu, measurements of total seeing or Fried parameter obtained during 1999, 2000, and 2001 are to some extent consistent with the stability and instability conditions represented by $1/R_i$. In particular, 1999 June has a high Fried parameter value in agreement with the weak intensity of $1/R_i$ in the free atmosphere of all studied months.

Table 2. Monthly statistics of the Fried parameter (r_0) of No.3 hill obtained by DIMM at the Gaomeigu site during 1999. Numbers of valid measurements are presented for each month (Qian et al. 2002).

Year	Month	No.	r_0 (cm)
1999	Feb	369	12.68
1999	Mar	266	10.31
1999	Apr	788	10.59
1999	May	180	9.83
1999	June	47	14.69
1999	July	36	12.11
1999	Dec	183	12.84

Table 3. Monthly statistics of the seeing (ε) and Fried parameter (r_0) obtained by DIMM at the Gaomeigu site during the period of 2000 and 2001. Numbers of valid measurements are presented for each month (Cen et al. 2002).

Year	Month	No.	r_0 (cm)	ε (arcsec)
2000	Oct	342	10.95	1.00
2000	Nov	875	10.77	1.02
2000	Dec	444	11.48	0.96
2001	Mar	195	11.76	0.94
2001	May	32	11.95	0.92
2001	July	52	15.10	0.73

Moreover, in 2001 July, good seeing is observed in accordance with the low value of $1/R_i$ in the free atmosphere. We conclude that the estimates of Richardson maps match the measurements by differential image motion monitor (DIMM). This implies that the measurements by DIMM agree with the estimates of Richardson maps representing stable and unstable conditions in the atmosphere.

5.2 Refractive index structure constant C_n^2

R_i is a satisfying indicator of development of optical turbulence, but it cannot be used to quantify the intensity of optical turbulence at a precise height. The quantification of the strength of turbulence is crucial for astronomical site characterization. In order to achieve this purpose, average vertical profiles of C_n^2 calculated with ERA5 data at Gaomeigu and Lhasa station are presented. Then, the estimations are compared with the coinciding measurements obtained from instrumented balloons.

To estimate the C_n^2 profile from ERA5 data, the Tatarskii equation is used, according to equation (5) (Tatarskii 1961):

$$C_n^2 = 2.8 L_0^{4/3} M^2, \tag{3}$$

where L_0 (in m) is the outer scale for optical turbulence. M (equation 6) is the gradient of potential refractive index (in m^{-1}) provided by Coulman et al. (1988) and θ (equation 7) is the potential temperature (in K), where P is the atmospheric pressure expressed in hPa and T is the absolute temperature:

$$M = \frac{\partial N}{\partial h} = -\frac{79 \times 10^{-6} P}{T^2} \frac{\partial \theta}{\partial h}, \tag{4}$$

$$\theta = T \left(\frac{1000}{P} \right)^{0.286}, \tag{5}$$

In addition, we estimate L_0 by two different outer-scale models. One was first proposed by Brown & Beland (1988) for altitudes between 17 and 30 km a.s.l., and it was later supplemented by Coulman et al. (1988) in the altitude range of 2000–17 000 m a.s.l.; it is only a function of altitude. For convenience, equations (8) and (9) are referred to as the C–V model:

$$L_0(h) = \frac{4}{1 + \left(\frac{h-8500}{2500} \right)^2}, 2000 \le h \le 17\,000\,\mathrm{m}, \tag{6}$$

$$L_0(h) = 0.307 - 0.0324(h-17) + 0.001\,67(h-17)^2 + 0.000\,476(h-17)^3, 17 \le h \le 30\,\mathrm{km}. \tag{7}$$

The other model is the HMNSP99 model (HMN model, equation 10), given by Ruggiero & DeBenedictis (2002), containing wind-speed shear and gradient of absolute temperature:

$${L_0}^{4/3}(h) = \begin{cases} 0.1^{4/3} \times 10^{0.362 + 16.728 \times S - 192.347 \frac{dT}{dh}}, & \text{troposphere} \\ 0.1^{4/3} \times 10^{0.757 + 13.819 \times S - 57.784 \frac{dT}{dh}}, & \text{stratosphere} \end{cases}, \tag{8}$$

$$S = \left[\left(\frac{\partial u}{\partial h} \right)^2 + \left(\frac{\partial v}{\partial h} \right)^2 \right]^{1/2}. \tag{9}$$

A comparison of the average C_n^2 profile at Gaomeigu and Lhasa station between the estimations using different outer-scale models based on ERA5 data and the corresponding measurements accquired from radiosondes is shown in Fig. 9. The radiosonde data for these sites are available for several days in 2013 April for Gaomeigu and in 2018 August for Lhasa station, and readers can refer to Wu et al. (2014) and Han et al. (2020) for detailed information. The specific hours of ERA5 data used to calculated C_n^2 profile are as close as possible to those of launching balloons. In addition, we present the C_n^2 profile of the widely known standard model, Hufnagel (1974), on the same figure. From Fig. 9, for Gaomeigu, we conclude that the C_n^2 profile calculated with the ERA5 system has a similar trend to the average profile of C_n^2 detected by balloons. Particularly for the C_n^2 profile obtained by the HMN model, it is more consistent with the measurement than other models at Gaomeigu. However, for Lhasa station, there exist some differences in trend and amplitude between estimations and observation. This implies that the turbulence outer-scale models used in this study cannot reveal the turbulence characteristics at Lhasa station very well. Therefore, choosing a suitable outer-scale model is critical in estimating turbulence strength.

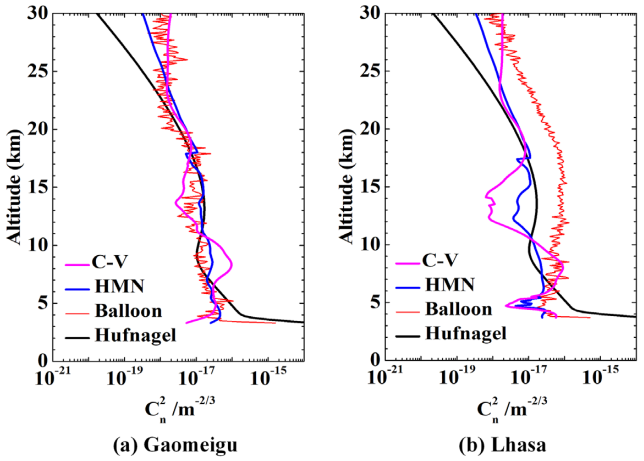

Figure 9. Comparison of vertical profiles of average C_n^2 calculated from ERA5 data with the measurement obtained by radiosondes at Gaomeigu and Lhasa station. The estimations of C_n^2 profile are calculated by the HMN, C–V, and Hufnagel models, respectively.

6 CONCLUSIONS AND DISCUSSIONS

In this study, our aim was to present the vertical distribution of the wind speed and optical turbulence above Gaomeigu and the Tibetan Plateau, for astronomical applications. We have utilized the ERA5 archives retrieved from the nearest grid point to Gaomeigu and Lhasa station above the Tibetan Plateau to investigate the distribution of vertical wind speed on a 20-yr time-scale (1999–2018). At the same time, we have compared the stability and instability of the free atmosphere and estimated the C_n^2 profiles at the two sites. Our results and conclusions are presented as follows:

(1) The statistical analysis has verified that the atmospheric parameters (wind speed, absolute temperature) in the free atmosphere retrieved from ERA5 data coincide with measurements obtained from IGRAv2 at Tengchong and Lhasa stations, with a satisfactory level of reliability.

For these two sites, the absolute temperature presents a bias and RMSE basically within 1.2 K. The wind speed has a bias and RMSE basically within 1.5 m s^{-1} and 2 m s^{-1}, respectively.

(2) We have provided monthly median distributions of vertical wind speed in the atmosphere over 20 years (1999–2018) above Gaomeigu and Lhasa station. From autumn to spring, with the exception of September, the wind speeds show representative features of mid-latitude sites with a noticeable maximum wind-speed value at the jet-stream level (200 hPa), about 12 km a.s.l. above the two sites.

During summer and September, the wind speeds are weaker than in other months and show different trends for the two sites. In June and

September, the median wind speed never exceeds 17 m s^{-1} within 5–30 km a.s.l. above the two sites. In particular, in September at Gaomeigu, the maximum median wind speed is not greater than 5 m s^{-1} below 12 km a.s.l.

In general, during January to April and July and August, the strength of wind speed at Gaomeigu is basically higher than or equal to that of Lhasa station, while in other months, the relationship of the wind-speed intensity above the two sites is complex.

The profiles of monthly median wind speed present clear seasonal behaviour, with stronger wind speeds during winter and weaker ones during summer and September.

In the same period, the monthly average wind speed at 200 hPa is presented. The wind speeds at the height of the jet-stream level also show significant seasonal fluctuations. For Gaomeigu, the highest average wind speed at 200 hPa is observed in January with a value of 53.02 m s^{-1}, while the lowest average wind speed is found in September with a value of 4.83 m s^{-1}. For Lhasa station, the strongest and weakest average wind speeds at 200 hPa are found in January (53.57 m s^{-1}) and July (4.74 m s^{-1}).

(3) The Richardson number maps of the free atmosphere above Gaomeigu and Lhasa station provide us with the relative possibility of atmospheric turbulence being produced in different periods and in different regions. For the two sites, during summer and September, atmospheric turbulence is not easily induced. In general, the condition of the atmosphere at Gaomeigu is more stable than that at Lhasa station. Especially in June, a regime of atmospheric stability within 6–30 km a.s.l. at Gaomeigu is basically superior or equal to the stable condition found at two mid-latitude sites, Oukaimeden and La Palma, during the same period.

(4) We have provided average C_n^2 profiles over Gaomeigu and Lhasa station obtained from the ERA5 data. The estimations of C_n^2 profiles using different outer scales present similar tendencies to the balloon measurements at Gaomeigu, especially for the HMN model. However, for Lhasa station, there exist some differences in trend and amplitude between estimations and measurements. Therefore, the two outer scales used in this study cannot better reveal the local turbulence characteristics at Lhasa station. These results imply that choosing a suitable outer-scale model that can reveal the nature of local turbulence chatacteristics is crucial for estimating the turbulence intensity.

ACKNOWLEDGEMENTS

The authors are grateful to the anonymous referee for valuable remarks that helped to improve and clarify this manuscript. This work was supported by the National Natural Science Foundation of China (Grant No. 91752103), the Strategic Priority Research Program of the Chinese Academy of Sciences (Grant No. XDA17010104), and the Foundation of the Key Laboratory of Science and Technology Innovation of the Chinese Academy of Sciences (Grant No. CXJJ-19S028).

DATA AVAILABILITY

The ERA5 data are available in the Copernicus Climate Change Service Climate Data Store (CDS), at https://cds.climate.copernicus.eu/cdsapp#!/home. Radiosoundings are obtained from https://www.ncdc.noaa.gov/data-access/weather-balloon/integrated-global-radiosonde-archive.

REFERENCES

Abahamid A., Jabiri A., Vernin J., Benkhaldoun Z., Azouit M., Agabi A., 2004, A&A, 416, 1193
Avila R., Vernin J., Sánchez L., 2001, A&A, 369, 364
Avila R., Carrasco E., Ibanez F., Vernin J., Prieur J. L., Cruz D. X., 2006, PASP, 118, 503
Azouit M., Vernin J., 2005, PASP, 117, 536
Bao X. H., Zhang F. Q., Sun J. H., 2011, Mon. Weather Rev., 139, 2790
Bolbasova L. A., Shikhovtsev A. Y., Kopylov E. A., Selin A. A., Lukin V. P., Kovadlo P. G., 2019, MNRAS, 482, 2619
Brown J. H., Beland R. R., 1988, Phys. Scr., 37, 424
Caccia J. L., Azouit M., Vernin J., 1987, Applied Opt., 26, 1288
Cai J., Li X. B., Zhan G. W., Wu P. F., Xu C. Y., Qing C., Wu X. Q., 2018, Acta Phys. Sinica, 67, 014206
Cen X. F., Qian T. L., Wang J. C., Wang C. Y., 2002, Publ. Yunnan Obs., 92, 45
Coulman C. E., Vernin J., Coqueugniot Y., Caccia J. L., 1988, Applied Opt., 27, 155
Ding Y., Chan J. C. L., 2005, Meteorology Atmos. Phys., 89, 117
Durre I., Vose R. S., Yin X., Applequist S., Arnfield J., 2016, Integrated Global Radiosonde Archive (IGRA) Version 2. Available at https://data.nodc.noaa.gov/cgi-bin/iso?id=gov.noaa.ncdc:C00975#
Egner S. E., Masciadri E., McKenna D., 2007, PASP, 119, 669
Fried D. L., 1966, J. Opt. Soc. America, 56, 1372
García-Lorenzo B., Fuensalida J. J., Muñoz-Tuñón C., Mendizabal E., 2005, MNRAS, 356, 849
García-Lorenzo B., Eff-Darwich A., Fuensalida J. J., Castro-Almazán J., 2009, MNRAS, 397, 1633
Geissler K., Masciadri E., 2006, PASP, 118, 1048
Gelaro R. et al., 2017, J. Climate, 30, 5419
Habib A., Vernin J., Benkhaldoun Z., 2005, Comptes Rendus Phys., 6, 385
Hach Y., Jabiri A., Ziad A., Bounhir A., Sabil M., Abahamid A., Benkhaldoun Z., 2012, MNRAS, 420, 637
Hagelin S., Masciadri E., Lascaux F., Stoesz J., 2008, MNRAS, 387, 1499
Hagelin S., Masciadri E., Lascaux F., 2010, MNRAS, 407, 2230
Han Y. et al., 2020, J. Opt. Soc. America A, 37, 995
Hersbach H. et al., 2020, Q. J. R. Meteorological Soc., 1
Huang Y. L., 1996, Publ. Yunnan Obs., 1, 12
Hufnagel R. E., Stanley N. R., 1964, J. Opt. Soc. America, 54, 52
Hutt D. L., 1999, Opt. Eng., 38, 1288
Kobayashi S. et al., 2015, J. Meteorological Soc. Jpn. Series II, 93, 5
Kuo C. L., 2017, Astrophys. J., 848, 64
Liu L. et al., 2012, Ground-Based and Airborne Telescopes IV. International Society for Optics and Photonics, Amsterdam, Netherlands, p. 844464
Liu Z. Z., Luan D., Yu J. M., Ma K. Q., Long K., Zhang Z. S., 1999, Publ. Yunnan Obs., 1, 42
Li Y., Qian S. B., 2005, in Sterken C., ed., ASP Conf. Ser. Vol. 335, The Light-Time Effect in Astrophysics: Causes and Cures of the O–C Diagram. Astron. Soc. Pac., San Francisco, p. 245
Ma K. Q., Luan D., Liu Z. Z., Long K., Zhang Z. S., Li Y. l., Yu J. M., 1996, Publ. Yunnan Obs., S1, 42
Masciadri E., Garfias T., 2001, A&A, 366, 708
Masciadri E., Stoesz J., Hagelin S., Lascaux F., 2010, MNRAS, 404, 144
Masciadri E., Lascaux F., Fini L., 2013, MNRAS, 436, 1968
Qian T. L., Li Y. L., Shang Q. Z., Xu J., Qin X. F., 1996, Publ. Yunnan Obs., S1, 57
Qian T. L., Wang C. Y., Cen X. F., Wang J. C., 2002, Publ. Yunnan Obs., 2, 75
Qian X., Yao Y., Wang H., Wang Y., Bai Z., Yin J., 2018, PASP, 130, 125002
Roddier F., 1981, in Wolf E., ed., Progress in Optics. Elsevier, Amsterdam, p. 281
Ruggiero F. H., DeBenedictis D. A., 2002, Forecasting Optical Turbulence from Mesoscale Numerical Weather Prediction Models. DOD High Performance Computer Users Group Conference, Austin Texas , p. 10
Saha S. et al., 2014, J. Climate, 27, 2185
Sarazin M., Tokovinin A., 2002, in Vernet E., Ragazzoni R., Esposito S., Hubin N., eds., ESO Conf. Workshop Proc. Beyond Conventional

Adaptive Optics: A Conference Devoted to the Development of Adaptive Optics for Extremely Large Telescopes, ESO, Garching, Germany, p. 321
Stone R., 2012, Science, 337, 1156
Tatarskii V. I., 1961, Wave Propagation in Random Media. McGraw-Hill, New York
VanZandt T. E., Green J. L., Gage K. S., Clark W. L., 1978, Radio Sci.., 13, 819
VanZandt T. E., Gage K. S., Warnock J. M., 1981, Proc. 20th Conf. Radar Meteorology. American Meteorological Society, Boston, MA, p. 129
Venemans B., 2015, Nature, 518, 490
Vernin J., 1986, Astronomical Site Selection: A New Meteorological Approach. Advanced Technology Optical Telescopes III, Tucson, USA, p. 142
Vernin J., Azouit M., 1983, J. Opt., 14, 5
Wang C. J. et al., 2019, Res. Astron. Astrophys., 19, 149
Wu X. et al., 2015, Nature, 518, 512
Wu X. Q., Qian X. M., Huang H. H., Wang P., Cui C. L., Qing C., 2014, Acta Astron. Sinica, 55, 144
Yao Y., Wang H., Liu L., Wang Y., Qian X., Yin J., 2012, Ground-Based and Airborne Telescopes IV. International Society for Optics and Photonics, Amsterdam, Netherlands, p. 84441K
Yao Y., Zhou Y., Liu L., Wang H., Yin J., You X., Fu X., 2015, J. Phys. Conf. Series, 595, 012038
Ye Q., Su M., Li H., Zhang X., 2016, MNRAS, 457, L1
Yu J. M., Liu Z. Z., Luan D., Long K., Ma K. Q., Zhang Z. S., 1996, Publ. Yunnan Obs., 1, 48
Yunnan Observatory Site Survey Group, 1999a, Acta Astron. Sinica, 40, 319
Yunnan Observatory Site Survey Group, 1999b, Acta Astron. Sinica, 40, 326
Zhang B. R., Yu J. M., Tan H. S., 1996, Publ. Yunnan Obs., 1, 1
Zhang Y., Wang P., Yao Y., Wang G., Liu L., Qian X., 2010, Sci. Sinica Phys. Mech. Astron., 40, 1302

SUPPORTING INFORMATION

Supplementary data are available at *MNRAS* online.

appendix_MN-20-2284-MJ.R2_0923.docx

Please note: Oxford University Press is not responsible for the content or functionality of any supporting materials supplied by the authors. Any queries (other than missing material) should be directed to the corresponding author for the article.

APPENDIX A:

Monthly average of wind speed at 200 hPa from ERA5 data during 1999–2018 at Gaomeigu and Lhasa station is shown in Tables A1 and A2 in Appendix A.

Table A1. Monthly average of wind speed at 200 hPa from ERA5 data during 1999–2018 at Gaomeigu.

Month	h (km)	Average (m s^{-1})
Jan	12.18	53.02
Feb	12.18	50.66
Mar	12.20	46.00
Apr	12.27	38.16
May	12.41	23.46
June	12.51	7.68
July	12.53	9.77
Aug	12.53	9.23
Sept	12.50	4.83
Oct	12.41	23.02
Nov	12.29	42.11
Dec	12.23	49.39

Table A2. Monthly average of wind speed at 200 hPa from ERA5 data during 1999–2018 at Lhasa station.

Month	h (km)	Average (m s^{-1})
Jan	12.03	53.57
Feb	12.04	50.83
Mar	12.08	43.56
Apr	12.18	34.76
May	12.34	28.00
June	12.49	13.17
July	12.56	4.74
Aug	12.55	5.68
Sept	12.49	10.25
Oct	12.33	33.67
Nov	12.18	48.13
Dec	12.10	53.07

APPENDIX B:

A comparison of the lowest monthly median vertical profiles of 1/Ri found at Gaomeigu Oukaimeden and La Palma is shown in Fig. B1 in Appendix B.

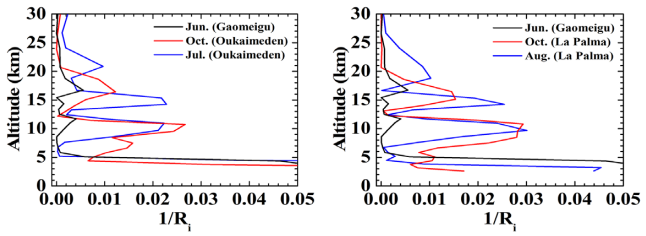

Figure B1. A comparison of the lowest monthly median vertical profiles of $1/R_i$ found at Gaomeigu in June, Oukaimeden in July and October, and La Palma in August and October during 1999–2018. The data are retrieved from the ERA5 data.

This paper has been typeset from a Microsoft Word file prepared by the author.